A robotic system for ^{18}F-FMISO PET-guided intratumoral pO_2 measurements

Jenghwa Chang[a] and Bixiu Wen
Department of Medical Physics, Memorial Sloan Kettering Cancer Center, 1275 York Avenue, New York, New York 10021

Peter Kazanzides
Department of Computer Science, The Johns Hopkins University, 3400 North Charles Street, Baltimore, Maryland 21218

Pat Zanzonico
Department of Medical Physics, Memorial Sloan Kettering Cancer Center, 1275 York Avenue, New York, New York 10021

Ronald D. Finn
Department of Radiology, Memorial Sloan Kettering Cancer Center, 1275 York Avenue, New York, New York 10021

Gabor Fichtinger
Department of Computer Science, The Johns Hopkins University, 3400 North Charles Street, Baltimore, Maryland 21218 and School of Computing, Queen's University, 25 Union Street, Kingston, Ontario, K7L 3N6 Canada

C. Clifton Ling
Department of Medical Physics, Memorial Sloan Kettering Cancer Center, 1275 York Avenue, New York, New York 10021 and Varian Medical Systems, 3100 Hansen Way, Palo Alto, California 94304

(Received 19 December 2008; revised 20 August 2009; accepted for publication 3 September 2009; published 20 October 2009)

An image-guided robotic system was used to measure the oxygen tension (pO_2) in rodent tumor xenografts using interstitial probes guided by tumor hypoxia PET images. Rats with ~1 cm diameter tumors were anesthetized and immobilized in a custom-fabricated whole-body mold. Imaging was performed using a dedicated small-animal PET scanner (R4 or Focus 120 microPET™) ~2 h after the injection of the hypoxia tracer ^{18}F-fluoromisonidazole (^{18}F-FMISO). The coordinate systems of the robot and PET were registered based on fiducial markers in the rodent bed visible on the PET images. Guided by the 3D microPET image set, measurements were performed at various locations in the tumor and compared to the corresponding ^{18}F-FMISO image intensity at the respective measurement points. Experiments were performed on four tumor-bearing rats with 4 (86), 3 (80), 7 (162), and 8 (235) measurement tracks (points) for each experiment. The ^{18}F-FMISO image intensities were inversely correlated with the measured pO_2, with a Pearson coefficient ranging from −0.14 to −0.97 for the 22 measurement tracks. The cumulative scatterplots of pO_2 versus image intensity yielded a hyperbolic relationship, with correlation coefficients of 0.52, 0.48, 0.64, and 0.73, respectively, for the four tumors. In conclusion, PET image-guided pO_2 measurement is feasible with this robot system and, more generally, this system will permit point-by-point comparison of physiological probe measurements and image voxel values as a means of validating molecularly targeted radiotracers. Although the overall data fitting suggested that ^{18}F-FMISO may be an effective hypoxia marker, the use of static ^{18}F-FMISO PET postinjection scans to guide radiotherapy might be problematic due to the observed high variation in some individual data pairs from the fitted curve, indicating potential temporal fluctuation of oxygen tension in individual voxels or possible suboptimal imaging time postadministration of hypoxia-related trapping of ^{18}F-FMISO. © *2009 American Association of Physicists in Medicine*. [DOI: 10.1118/1.3239491]

Key words: hypoxia, small animal imaging, pO_2 measurement, image guidance, robot

I. INTRODUCTION

Solid tumors develop regions of hypoxia (i.e., chronic hypoxia) when they outgrow their blood supply, producing decreasing pO_2 gradients between the well-perfused normoxic areas and the poorly perfused hypoxic areas.[1,2] Detecting and quantifying oxygen levels in human tumors may be predictive of tumor responsiveness to radiation and certain chemotherapeutic agents and of clinical outcome. The presence of hypoxia in tumors has been established as an independent predictor of tumor progression and resistance to treatment.[3–9] Studies of tumor hypoxia may further our understanding of the malignant phenotype, tumor progression, radiation-induced reoxygenation, and treatment outcome.[10–12]

Oxygen partial pressure (pO_2) can be directly measured in

tumor and other tissues with oxygen-sensitive electrodes or fiber-optic probes.[13–16] These methods have obvious limitations in the clinical setting due to the inaccessibility of some tumors, the invasive nature of the procedure, and limited sampling. Another method—immunohistochemical analysis of tumor biopsies using either endogenous or exogenous tumor hypoxia markers—is also invasive and prone to sampling error. Tumor hypoxia may also be imaged noninvasively using radiolabeled hypoxic cell markers in combination with either single-photon emission computed tomography (SPECT) or positron emission tomography (PET).[17–21] In addition, magnetic resonance imaging (MRI) methods are being explored to yield information on tumor hypoxia.[22,23]

Misonidazole is an azomycin-based hypoxic cell sensitizer[24] that binds covalently to intracellular molecules at levels that are inversely related to intracellular oxygen concentration.[25] ^{18}F-fluoromisonidazole (^{18}F-FMISO), a PET imaging agent derived from misonidazole, is a freely diffusible agent and, in the absence of hypoxia, is nonspecifically distributed among tissues. ^{18}F-FMISO PET has been the most commonly used agent for clinical PET hypoxia imaging to date[25] and has been used to detect hypoxia in lung tumors, sarcoma, and head and neck cancers.[26] Based on clinical and laboratory findings with ^{18}F-FMISO hypoxia imaging, the optimal time for imaging appears to be between 90 and 120 min postinjection.[25] This time point has been widely adopted for clinical hypoxia imaging using ^{18}F-FMISO.[19,27]

Although noninvasive imaging of tumor hypoxia with PET has many advantages, it is an indirect method subject to various confounding factors.[20,28] Given that direct pO_2 measurements have been correlated with treatment outcome,[29] it is desirable to compare PET-based hypoxia imaging to pO_2 probe data as a means of validation. However, to date, attempts to compare PET-based hypoxia imaging to ^{18}F-FMISO and Eppendorf measurement in clinical studies have shown a notable absence of correlation.[30,31] This is perhaps due to misregistration of the probe measurement and image positions as well as acute hypoxia (short-term fluctuations in pO_2 produced by intermittent opening and closing of tumor blood vessels).[32]

To overcome shortcomings of comparison of nonregistered point measurements and voxel image intensities, we developed a template system to manually register PET image intensity in rodent tumors with pO_2 values measured using an OxyLite™ fiber-optic probe.[20] Although the latter provides fine spatial sampling (i.e., the probe tip is 220 μm in diameter), manual registration is labor intensive, time consuming, and ultimately unreliable. An automated image-guided robotic system therefore offers distinct advantages in accuracy and minimal invasiveness that are difficult to achieve with manual operation. Recently, investigators have explored the clinical use of robotic systems in surgery, radiotherapy, and biopsy procedures.[33–37] However, image-guided robotic systems for small-animal studies remain scarce. Needle-positioning robots for image-guided interventions in small-animal research models have been reported for biopsy and *in vivo* measurement by our group[38] and others.[39,40] Our image-guided robotic system was evaluated as a more reliable alternative to manual probe placement to thereby improve the accuracy as well as efficiency of probe-based validation of hypoxia imaging agents. Design and validation of this system using a phantom have been reported.[38]

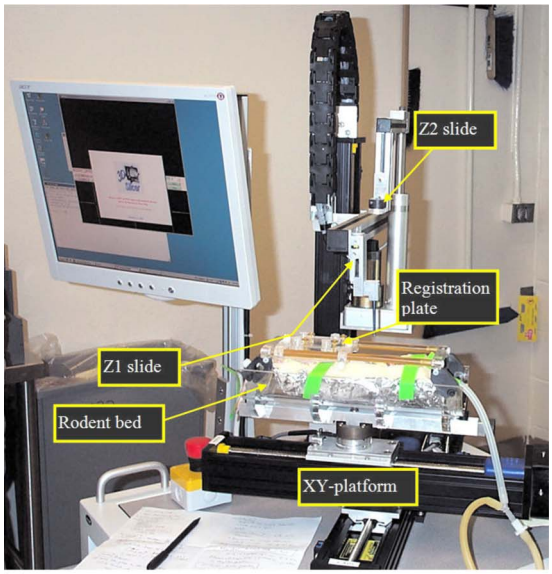

(a)

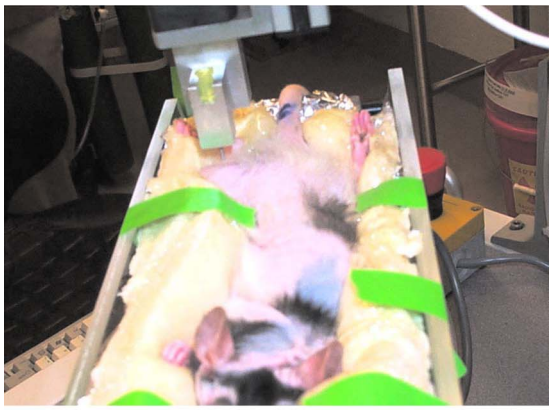
(b)

FIG. 1. (a) The image-guided robot system. (b) Image-guided measurement of oxygen level using the Oxylite probe.

In the current study, we evaluated the utility of our robotic system in image-guided probe measurement of pO_2 levels in tumors in live animals. Specifically, the oxygen levels in a rat prostate adenocarcinoma growing in the hindlimbs of nude rats were measured using an OxyLite™ probe, guided by ^{18}F-FMISO PET images. We report in this paper the correlation between the PET image intensities and the measured pO_2 values to evaluate the accuracy of the PET hypoxia image and spatial correlation between pO_2 values and tumor hypoxia visualized with immunofluorescent staining.

II. IMAGE-GUIDED ROBOT SYSTEM

A detailed description and evaluation of this image-guided robot system using a phantom has been provided in a previous publication.[38] Briefly, as shown in Fig. 1(a), the

robot system consists of an *X-Y* horizontal platform and two vertical (Z1 and Z2) slides. An arm is attached to the Z1 slide to hold either the registration "touch" probe (for spatially registering the robot and PET-image coordinate systems) or the cannula with the pO_2 probe in place. A removable registration plate can be mounted on the rodent holder. The plate includes four small wells (each ~5 μl in volume) to which a drop of a high-activity concentration PET-visible radiotracer (e.g., ^{18}F-FMISO) can be added to serve as fiducial markers for registration between the imaging and the robot coordinate systems. For pO_2 measurements [Fig. 1(b)], the operator specifies points of interest along multiple tracks in the image space using the visualization software. The software transforms the measurement positions from image to robot coordinates and sequentially performs probe measurements at the preprogramed positions (depth increments) along each track.

The positional error of the robotic system was previously studied using fiducial markers and a phantom.[38] The results indicated that the robot system could position the measurement probe at a defined target point with a mean error of less than 0.4 mm. Since the phantom study did not account for the error due to nonrigid deformation of the animal body induced by the insertion and the manipulation of the probe, the 0.4 mm error represents a lower bound of achievable positional accuracy for this robot system.

III. EXPERIMENT

III.A. Animal preparation

Four experiments were performed on four rats. All animal procedures complied with the applicable guidelines of Memorial Sloan-Kettering Cancer Center (MSKCC) and were performed under the auspices of an experimental protocol approved by the MSKCC Institutional Animal Care and Use Committee (IACUC). The syngeneic Dunning R3327-AT anaplastic prostate adenocarcinoma growing in nude rats was used as the tumor model. Tumors were initiated by subcutaneous injection of approximately 2×10^6 cells in the right hind leg. Following injection, the rats were periodically examined and the tumor dimensions were measured. At the time of PET imaging and the pO_2 measurements, at 2 week postimplantation, the tumor had grown to approximately 2 cm in diameter.

For experiments, an animal-specific custom-fabricated foam mold (Rapid-Foam™, Soule Medical, Lutz, FL), which fits into the rodent bed, was fabricated to immobilize the animal.[41] The mold was fabricated in place in the animal holder, temporarily (i.e., only for the fabrication procedure) lined with aluminum foil, and can easily be removed from and replaced back in the holder.

III.B. MicroPET scan

^{18}F-fluoride was produced in the MSKCC cyclotron (EBCO Technologies, Inc., Vancouver, Canada) by proton irradiation of an enriched ^{18}O-water target in a small-volume titanium chamber. ^{18}F-FMISO was prepared as reported[42,43] with minor modifications. The animal was anesthetized (induction phase of 2.0% isoflurane and maintenance phase of 1.0% with air as the carrier gas) and placed in the prone position in its custom-fabricated mold. ^{18}F-FMISO [63 MBq (1.7 mCi)] was intravenously administered via bolus injection through the tail vein. The first animal was scanned on the R4 microPET™ and the other three on the Focus 120 microPET™. At 2 h postadministration, two scans were performed. The first image acquisition lasted for 5 min, recording a minimum of 20 million events over the tumor-bearing hindlimb region. The longitudinal position (±0.1 mm) of the animal bed for imaging, given by a digital display on the microPET™ control console, was recorded. The animal bed was then retracted out of the imaging gantry and a drop of solution containing ^{18}F-FMISO with an activity concentration of ~500 μCi/ml dispensed into each of the four fiducial-marker wells. The animal bed was then translated back into the imaging gantry to precisely the same position as for the first image and a second image acquired for 1 min. The resulting list-mode data were sorted into 2D sinogram by Fourier rebinning and transverse images reconstructed by filtered backprojection using a ramp filter with a cut-off frequency equal to the Nyquist frequency; no attenuation, scatter, or partial-volume correction were applied. The R4 and Focus 120 microPET scans were reconstructed in $128\times128\times64$ (voxel size of $0.85\times0.85\times1.21$ mm^3) and $128\times128\times96$ (voxel size of $0.87\times0.87\times0.80$ mm^3) volumes, respectively. The two image sets in each experiment were acquired in this sequence without and then with activity in the fiducial-marker indentations to avoid reconstruction artifacts (e.g., streaking) associated with the foci of concentrated activity when correlating the PET images with the pO_2 measurements.

III.C. Oxylite measurement

Tumor pO_2 was measured with a four-channel fiber-optic oxygen-sensitive device with a needle-type probe (OxyLite™ 4000, Oxford Optronix, Oxford, UK) as described previously.[44] This system converts the measured signals to pO_2 values in mm Hg using individual probe calibration data provided by the manufacturer. The pO_2 signal from OxyLite™ probe was averaged every 5 s and the pO_2 value was recorded in real time using a data-acquisition system (PowerLab® ADInstruments, Chart 4.2).

Immediately following completion of PET imaging and with the animal anesthetized and in place in the rodent holder, the registration probe was attached to the Z1 slide and moved under force-controlled mode to mate with the four fiducial marker wells and thus determine their positions in the robot space. The locations of fiducial markers in the PET image were then coregistered with those in the robot space.[38]

Three to eight tracks within the tumor were selected for measurement for each experiment. For each track, the start and end positions, and the increment (usually 0.5 mm) between sequential measurements were specified. For each track, the software first drove the robot to the entrance point of that track on the dorsal skin surface overlying the tumor

and the operator used a 24G3/4 gauge needle to puncture the skin and the underlying fascia, creating a channel for the cannula. The cannula was then attached to the Z1 slide and positioned by the robot to penetrate the opening by ~1 mm, providing a rigid conduit for inserting and advancing the pO_2 measurement probe and avoiding bending or other mechanical deformations of the probe tip. The probe, mounted on the Z2 slide, was then inserted through the cannula and advanced incrementally to each programmed measurement point along the selected tracks.

The pO_2 measurements were made at the starting point of each track and subsequently at 0.5 mm steps until the specified end position was reached. To avoid artifacts due to pressure on its tip, the probe was retracted 0.3 mm after each incremental advance before initiating pO_2 measurement. Once the pO_2 reading at each position stabilized, the value was manually entered into the appropriate field of the visualization software. The measurement positions, image intensities, and pO_2 values along each track were exported for analysis.

III.D. Immunohistochemical staining and image acquisition

Immunohistochemical staining of the tumors was also performed for the first experiment. Pimonidazole (60 mg/kg), a standard maker for tissue hypoxia, was coadministered via tail vein injection with ^{18}F-FMISO. Hoechst 33342 (15 mg/kg), an immunofluorescent perfusion stain, was administered immediately after all pO_2 measurements had been completed and 1 min before the animal was sacrificed by carbon dioxide asphyxiation. The tumor was removed, immediately frozen in cryofixative, and microtomed into 8 μm thick sections with the sections cut perpendicularly to the direction of the first track.

The sections were immunohistochemically stained following the procedure described in an early publication[45] and scanned on an image analysis system consisting of a Zeiss BX40 fluorescence microscope using a computer-controlled motorized stage with a digital camera and METAMORE software 6.3. All images were scanned at 50× magnification. Composite images of the entire tumor were generated by the software from individual microscopic images. Sections were first imaged for Hoechst; then the same sections were stained for pimonidazole and scanned. Finally, the sections were stained with hematoxylin and eosin (H&E) and scanned.

IV. DATA ANALYSIS

IV.A. ^{18}F-FMISO binding curve

The reaction of ^{18}F-FMISO in the presence of oxygen is

$$R\text{-}NO_2^- \underset{e^-}{\overset{O_2}{\rightleftarrows}} R\text{-}NO_2, \tag{1}$$

where R-NO_2^- is the ^{18}F-FMISO compound and e^- is the free electrons. When the above equation reaches equilibrium, the concentrations of ^{18}F-FMISO and O_2 follow the following relation:

$$[R\text{-}NO_2^-]\cdot[O_2] = k\cdot([R\text{-}NO_2]_{max} - [R\text{-}NO_2^-])\cdot[e^-], \tag{2}$$

where k is the equilibrium constant and $[R\text{-}NO_2]_{max}$ is the maximum ^{18}F-FMISO concentration.

Then

$$[O_2] = -K_{50} + \frac{K_{50}\cdot[R\text{-}NO_2]_{max}}{[R\text{-}NO_2]}, \tag{3}$$

where $K_{50}=k[e^-]$ is the oxygen concentration when $[R\text{-}NO_2^-]$ is 50% of $[R\text{-}NO_2]_{max}$. Equation (3) indicates that the oxygen concentration is inversely related to the ^{18}F-FMISO concentration according to a rectangular hyperbolic function and was used to fit the ^{18}F-FMISO PET image intensity and measured pO_2 data.

IV.B. Data fitting

The image intensities and measured pO_2 values were plotted as a function of position along each track of measurement to validate the inverse correlation predicted by Eq. (3). Because each pO_2 datum is measured at a point but the microPET intensity represents a volume-averaged value of ^{18}F-FMISO activity in a voxel, a three-point moving average was performed on the pO_2 level along each track to best approximate the volume-averaging effect (voxel size $0.85\times0.85\times1.21$ mm^3 for the R4 and $0.87\times0.87\times0.80$ mm^3 for the Focus 120 microPET studies) Although the three-point average covers a length (1 mm) slightly larger than the voxel size, the average position coincides with the position of the center of the three measurement points being averaged. The correlation coefficient (Pearson product moment) of the image intensity versus pO_2 value was calculated for each track.

To obtain the overall correlation between pO_2 value and image intensity, a scatterplot of pO_2 versus image intensity was also generated using data from all tracks. According to the ^{18}F-FMISO-oxygen binding curve in Eq. (3), regression was performed to fit these data to a modified hyperbolic function,

$$y = -a + ax_{max}/x, \tag{4}$$

where y is the pO_2 level, x is the ^{18}F-FMISO image intensity, x_{max} is the maximum ^{18}F-FMISO image intensity, and $a=K_{50}$ is the regression coefficient. Because the maximum ^{18}F-FMISO image intensity was usually unknown and could not be reliably extrapolated from the scatter plot, the maximum ^{18}F-FMISO image intensity of the whole tumor in the PET scan was used for x_{max} in Eq. (4). Note that the maximum ^{18}F-FMISO image intensity was only a lower bound for the true x_{max}, which occurs only for very low oxygen tensions (in theory, $pO_2<5$ mm Hg). As a result, a was the only regression coefficient in Eq. (4) and represented an upper bound for K_{50}. The regression was carried out using the user-defined curve-fitting function of CURVEEXPER™ (Version 1.37) software.

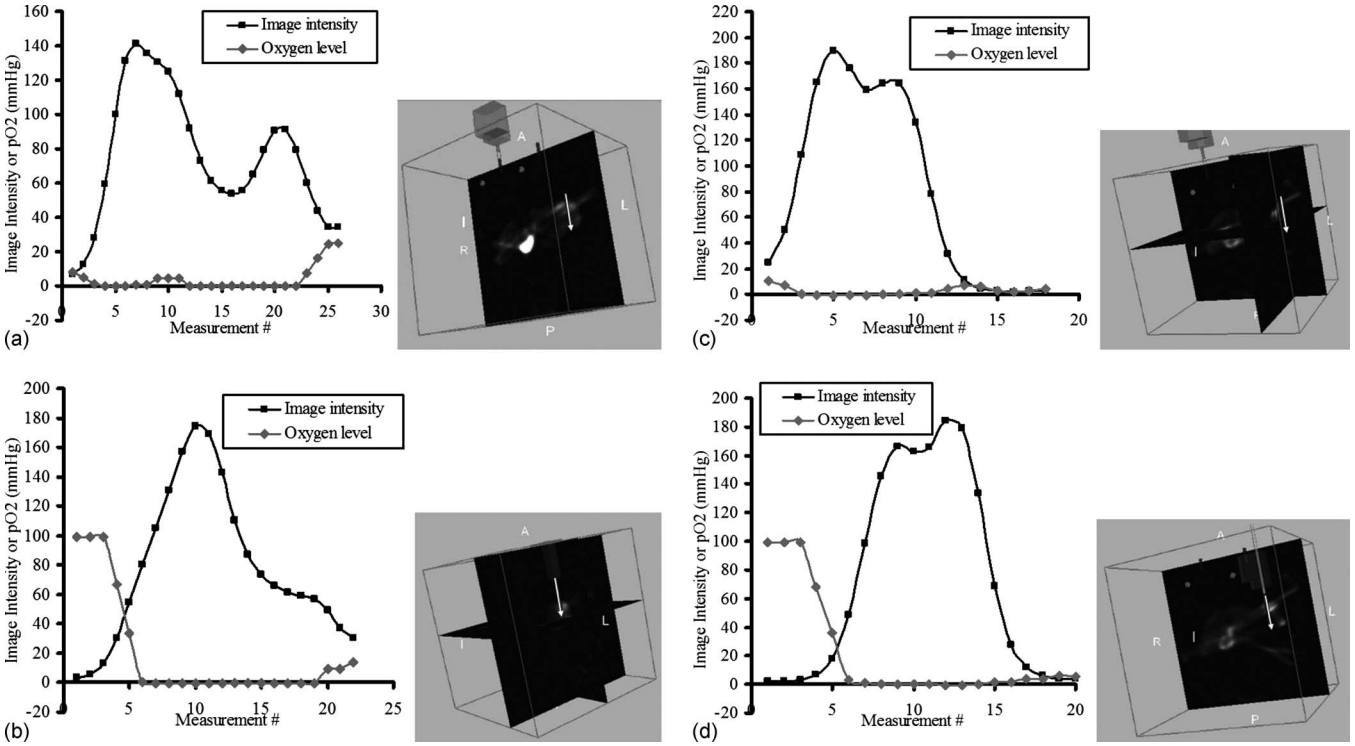

FIG. 2. Image intensity values and pO_2 measurements as a function of measurement point for the (a) first, (b) second, (c) third and (d) fourth tracks of the first experiment. Measurements were done every 0.5 mm. *R* is the Pearson product-moment correlation coefficient.

V. RESULTS

Point pO_2 values and corresponding ^{18}F-FMISO image intensities were successfully obtained for four tracks (86 measurement points) for the first rat, three tracks (80 measurement points) for the second rat, seven tracks (162 measurement points) for the third rat, and eight tracks (235 measurement points) for the fourth rat. The mean registration error between the robot and image coordinate systems was 0.15 mm with a standard deviation (SD) of 0.10 mm for the four experiments.

Figures 2(a)–2(d) present the image intensities and pO_2 values as a function of position (i.e., depth) for the four tracks of the first experiment. Correlation coefficients (Pearson product moment) of the image intensity value versus pO_2 (mm Hg) were also shown for each track. Similar results (not shown) were obtained for other experiments. Figures 3(a)–3(d) shows the scatterplot of pO_2 value versus image intensity using all data of each experiment. The gray curve is the best fit of the data to a modified hyperbolic function [Eq. (4)].

Tables I and II summarizes the data analysis results. Table I lists the Pearson product coefficients between ^{18}F-FMISO image intensity and measured pO_2 for each track of each experiment, as well as the mean and SD of the mean Pearson product coefficients ("mean of mean" and "SD of mean") of all four experiments. An inverse correlation was generally observed although the Pearson product coefficients varied significantly among experiments (the mean coefficient ranges from −0.60 to −0.83 for the four experiments with a mean and SD of −0.709 and 0.104, respectively) and within each experiment (the SD of three experiments are larger than the SD of mean). Table II lists K_{50} and *R* (correlation coefficient) for the data fitting of the scatterplot to the modified hyperbolic function [Eq. (4)] for each experiment.

Figures 4 and 5 show the results for the immunohistochemical staining study for two tumor sections along the track in Fig. 2(a). Because the inserted probe produces cutting artifacts, probe location could only be identified on these

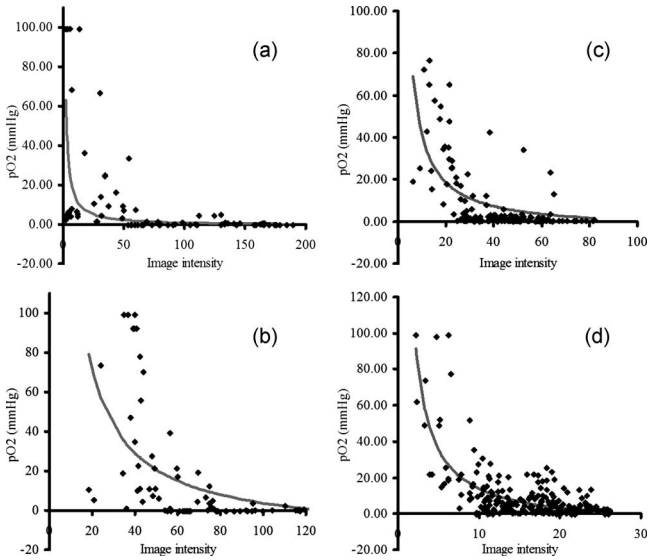

FIG. 3. Scatterplot of pO_2 versus image intensity for all tracks of (a) first, (b) second, (c) third, and (d) fourth experiments. Gray curve is the best fit of the data to a hyperbolic function. *R*: The correlation coefficient for the fit.

TABLE I. List of Pearson product coefficients between ^{18}F-FMISO image intensity and measured pO_2 for each track. (Mean of mean=−0.71, SD of mean=0.10, total mean=−0.71, total SD=0.19.)

Track	Animal 1	Animal 2	Animal 3	Animal 4
1	−0.41	−0.95	−0.81	−0.54
2	−0.66	−0.7	−0.97	−0.86
3	−0.76	−0.62	−0.86	−0.72
4	−0.55		−0.72	−0.77
5			−0.93	−0.70
6			−0.80	−0.88
7			−0.72	−0.14
8				−0.63
Mean	−0.60	−0.75	−0.83	−0.65
SD	0.15	0.17	0.10	0.24

two slices. The first section was estimated between measurement points 5 and 9 and the second section between measurement points 16 and 20. As shown in Fig. 4(a), the first probe location was in a viable tumor region, based on the H&E staining. Figure 4(b) indicates that the probe was positioned in a hypoxic region as demonstrated by intense pimonidazole staining and poor perfusion (i.e., no Hoechst 33324 staining). These results were consistent with the low (i.e., hypoxic) pO_2 measurements and high image intensity values shown for measurement points 5–9 of Fig. 2(a). The second probe location, on the other hand, was in a necrotic region because no viable tumor was observed by H&E staining of this region [Fig. 5(a)] and no pimonidazole or Hoechst 33342 staining was seen [Fig. 5(b)]. These results were also consistent with the low pO_2 measurements and low image intensity values for measurement points 16–20 of Fig. 2(a).

VI. DISCUSSION

Of the many methods for evaluating tumor hypoxia, probe-based pO_2 measurement, in being most direct, is generally regarded as a reference. PET imaging with exogenous hypoxic cell markers is less invasive and can yield 3D information, offering an attractive alternative in clinical application. To our knowledge, this is the first study that compares probe-based pO_2 measurement to image intensity of PET-based assessment of tumor hypoxia in a spatially registered "voxel-by-voxel" manner. Another important aspect is the use of a robotic system specifically designed for image-guided procedures as exemplified by this investigation. Not only did we demonstrate the feasibility of our approach and methodology, the direct comparison of pO_2 probe data with ^{18}F-FMISO PET image also yielded valuable insight regarding the use of these methods.

TABLE II. K_{50} and R (correlation coefficient) for the data fitting of the scatterplot to a hyperbolic function for each animal.

	K_{50}	R
Animal 1	0.6	0.52
Animal 2	13.2	0.48
Animal 3	4.0	0.64
Animal 4	7.7	0.73
Mean	6.4	0.60
SD	5.4	0.12

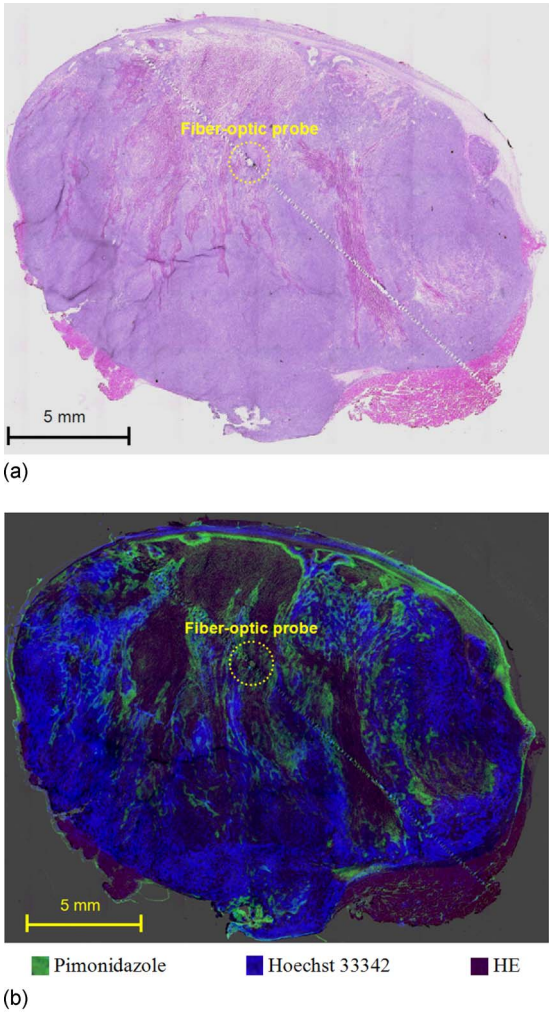

FIG. 4. Microscopic imaging study results for the slice containing measurement points 5–9 of Fig. 2(a). (a) HE stain. (b) Overlay of pimonidazole, Hoechst 33342, and HE stains. Circles are the location of the fiber-optic probe.

Bentzen *et al.*[31] did not observe any correlation between the average pO_2 and the ^{18}F-FMISO PET results in human cancers, which we believe is due to the lack of spatial registration of the two measured surrogates. In contrast, with the improved registration accuracy using our image-guided robotic system, we were able to observe reasonable correlation between probe-based pO_2 measurement and PET imaging with exogenous hypoxic cell markers. As shown in Table II, the average K_{50} was 6.4 ± 5.4 mm Hg in the Dunning R3327-AT tumor xenografts used in this study. This is in the range of oxygen tensions associated with radiobiological hypoxia, over which the oxygen enhancement ratio changes by several fold. Rasey *et al.*[46] observed for various cell lines that at oxygen tensions of 720–2300 ppm (2.6–8.32 mm Hg), FMISO binding was halfway between

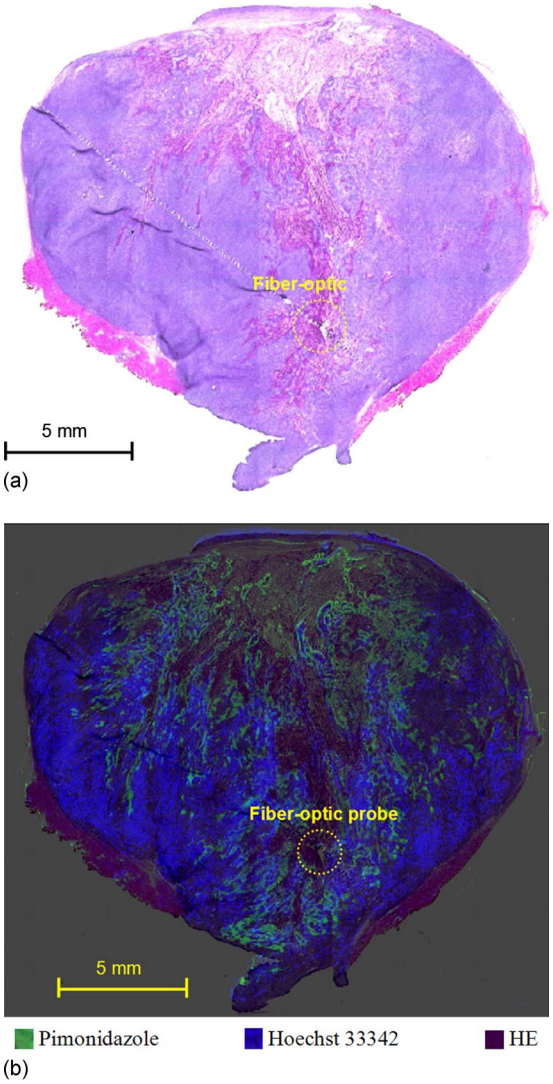

FIG. 5. Microscopic imaging study results for the slice containing measurement points 16–20 of Fig. 2(a). (a) HE stain. (b) Overlay of pimonidazole, Hoechst 33342, and HE stains. Circles are the location of the fiber-optic probe.

those under aerobic and anoxic conditions, respectively. Thus, the results of this study are consistent with the suggestion that FMISO is an effective marker for radiobiologically significant hypoxia and could potentially guide cancer radiotherapy, i.e., IMRT dose painting to hypoxia regions.

As presented in Table I, the measured pO_2 are negatively correlated with PET-FMISO image intensity, with Pearson coefficients ranging from −0.144 to −0.966 (with a mean and SD of −0.713 and 0.189, respectively) for the 22 tracks. The scattergram plots of the four experiments (Fig. 3) show significant data dispersion, that is, each probe-measured pO_2 level could correspond to a range of ^{18}F-FMISO image intensities instead of a single value and vice versa. Various factors that adversely affect the direct comparison of, and the inverse correlation between, probe-based pO_2 data and PET-FMISO image intensity are discussed below.

The two surrogates of tumor hypoxia in this study differ both spatially and temporally in their information content. Spatially, each microPET voxel represents a volume of ~0.6 or ~0.9 mm^3. In contrast, the detector element of the Oxylite is circular with a diameter of 220 μm. Thus, the signal in a microPET voxel represents that of a volume of over 70 000 cells (assuming that the diameter of cell is ~25 μm), orders of magnitude higher than that (~80 cells) provided by the Oxylite probe at its measurement positions. In terms of temporal resolution, the Oxylite yields the pO_2 level at discrete time points (i.e., at the instances of measurement), whereas the FMISO signal is the result of an integration over the period from tracer injection to image acquisition. In this regard, temporal changes in tumor hypoxia due to acute hypoxia,[32,47] leading to pO_2 fluctuation, could negatively affect the comparison between the Oxylite reading and the ^{18}F-MISO signal.

Tumor necrosis, known to exist in both animal and human tumors, is another confounding factor in relating probe-based pO_2 measurement to ^{18}F-FMISO image intensities. In fact, Figs. 4 and 5 clearly show the existence of necrosis in the Dunning R3327-AT anaplastic prostate adenocarcinoma used in this study. In the necrotic regions of the tumors, both surrogates (Hoechst 33342 and pimonidazole) would register low values of pO_2 because of the absence of functioning blood vessels, and ^{18}F-FMISO image intensity would be low because of the absence of viable hypoxic cells and of delivery of the radiotracer. The inclusion of the directly correlated pO_2 levels and ^{18}F-FMISO intensities recorded in such regions would compromise the expected inverse correlation. This can be understood in terms of the stained tissue sections in Figs. 4 and 5. The probe position in Fig. 4 was in a viable tumor region, and the measured pO_2 would follow the theoretical (hyperbolic) relation of inversely correlated pO_2 and image intensity, as described in Eqs. (3) and (4). The probe in Fig. 5, on the other hand, was in a necrotic region with both low image intensity and low pO_2 value. Of course, if such outliers can be excluded from the data analysis, the correlation would be improved (as will be discussed later).

There are two other factors of note, one being the uncertainty in spatially matching the probe position and the corresponding PET voxel, and the other being the influence of tracer delivery and pharmacokinetics on ^{18}F-FMISO PET signal intensity. The accuracy of registering the probe positions and PET voxels is affected by the reproducibility of tumor location between the two procedures. Recent data from our laboratory, applicable in part to this study, indicated that an uncertainty of 0.8 mm in repositioning the tumor in serial and prolonged imaging studies.[48] In this study, the possible bending of the Oxylite probe in penetrating the tumor may have introduced additional spatial uncertainty, although care was taken to reposition the probe if obvious bending was observed.

It is well established that both tumor physiology (i.e., blood flow, tracer delivery, washout, etc.) and pharmacokinetics (i.e., binding, dissociation, etc.) affect PET images, including those of tracers such as FDG and FMISO. For ^{18}F-FMISO PET imaging, Thowarth *et al.*[49] showed that images acquired at a given time point post-tracer injection may yield erroneous information on tumor hypoxia due to the

complex influence of physiology and pharmacokinetics. Such artifacts, of course, would also introduce dispersion in the comparison of probe-based and PET data.

We were aware that the above-discussed factors would influence the comparison of the two surrogates of tumor hypoxia, what was unknown was the extent to which the correlation will be affected. In this regard, the results of this study not only demonstrate correlation between probe-based pO_2 level and ^{18}F-FMISO PET image intensity but also provide a measure of the combined detrimental effects of these factors. In addition, in the course of our investigation we identified areas for improvement for future studies, as described below.

It is hypothesized that correlation between probe-based pO_2 level and ^{18}F-FMISO PET image intensity would be improved if data from necrotic volumes were excluded. For this purpose, we shall evaluate the use of dynamic contrast-enhanced MR imaging to distinguish perfused viable tissues and nonperfused necrotic tissues and systematically exclude spurious data.[50] To reduce spatial uncertainty due to the potential bending of the Oxylite probe, a more rigid metal needle probe (i.e., the Eppendorf™ pO_2 histography system) can be used, with the added advantage of speedier data acquisition using a stepping motor. Finally, we and others are investigating the use of dynamic ^{18}F-FMISO PET imaging and compartmental analysis to minimize the potential artifacts introduced by tumor physiology and pharmacokinetics.[49,51,52]

VII. SUMMARY

The use of advanced imaging techniques to elucidate the molecular basis of cancer is having a profound impact on cancer management. In this study, we used a novel image-guided robotic system to perform intratumoral pO_2 measurements spatially registered with hypoxia microPET images. Our results indicated that ^{18}F-FMISO PET image intensity is correlated with measured pO_2 and consistent with K_{50} values in the range of radiobiological hypoxia. Within the experimental uncertainties discussed previously, the results from this study support the use of ^{18}F-FMISO PET as a hypoxia surrogate, and this approach can be extended to validate the use of other PET hypoxia tracers. In addition, the image-guided robotic system provides a useful tool to perform other image-based procedures, e.g., delivery of hypoxia targeted therapeutics and biopsy of tumor specimens with specific image characteristics. In this regard, the present study provides a proof of principle and demonstration of feasibility of image-guided procedures in rodents using a robotic system specifically designed for such a purpose.

ACKNOWLEDGMENTS

Part of this work was presented at the 48th AAPM Annual Meeting, July 30–August 3, 2006, Orlando, FL. This work was partially supported by NIH under Grant Nos. RO1 CA84596 and P01 CA115675 and by NSF under Grant No. ERC 9731748. Technical services provided by the MSKCC Small-Animal Imaging Core Facility, supported in part by NIH Small-Animal Imaging Research Program (SAIRP) Grant No. R24 CA83084 and NIH Center Grant No. P30 CA08748, are gratefully acknowledged.

[a]Author to whom correspondence should be addressed. Electronic mail: jenghwachang@yahoo.com; Also at Department of Radiation Oncology, Tisch Hospital/NYU Langone Medical Center, 566 First Avenue TCH 114 HC, New York, NY 10016; Telephone: 212-263-2051; Fax: 212-263-5055.

[1]M. Hockel, P. G. Knapstein, and J. Kutzner, "A novel combined operative and radiotherapeutic treatment approach for recurrent gynecologic malignant lesions infiltrating the pelvic wall," Surg. Gynecol. Obstet. **173**, 297–302 (1991).

[2]P. Vaupel *et al.*, "Oxygenation of human tumors: Evaluation of tissue oxygen distribution in breast cancers by computerized O2 tension measurements," Cancer Res. **51**, 3316–3322 (1991).

[3]C. N. Coleman, "Hypoxia in tumors: A paradigm for the approach to biochemical and physiologic heterogeneity," J. Natl. Cancer Inst. **80**, 310–317 (1988).

[4]M. Hockel *et al.*, "Association between tumor hypoxia and malignant progression in advanced cancer of the uterine cervix," Cancer Res. **56**, 4509–4515 (1996).

[5]M. Hockel *et al.*, "Tumor oxygenation: A new predictive parameter in locally advanced cancer of the uterine cervix," Gynecol. Oncol. **51**, 141–149 (1993).

[6]M. Nordsmark *et al.*, "Hypoxia in human soft tissue sarcomas: Adverse impact on survival and no association with p53 mutations," Br. J. Cancer **84**, 1070–1075 (2001).

[7]M. Nordsmark, M. Overgaard, and J. Overgaard, "Pretreatment oxygenation predicts radiation response in advanced squamous cell carcinoma of the head and neck," Radiother. Oncol. **41**, 31–39 (1996).

[8]P. L. Olive, J. P. Banath, and C. Aquino-Parsons, "Measuring hypoxia in solid tumours—Is there a gold standard?," Acta Oncol. **40**, 917–923 (2001).

[9]P. Stadler *et al.*, "Influence of the hypoxic subvolume on the survival of patients with head and neck cancer," Int. J. Radiat. Oncol., Biol., Phys. **44**, 749–754 (1999).

[10]J. Chen *et al.*, "Expression of carbonic anhydrase 9 at the invasion front of gastric cancers," Gut **54**, 920–927 (2005).

[11]J. L. Spivak, "The anaemia of cancer: Death by a thousand cuts," Nat. Rev. Cancer **5**, 543–555 (2005).

[12]K. K. To *et al.*, "Genetic instability: The dark side of the hypoxic response," Cell Cycle **4**, 881–882 (2005).

[13]J. Bussink *et al.*, "Effects of nicotinamide and carbogen on oxygenation in human tumor xenografts measured with luminescense based fiber-optic probes," Radiother. Oncol. **57**, 21–30 (2000).

[14]D. R. Collingridge *et al.*, "Measurement of tumor oxygenation: A comparison between polarographic needle electrodes and a time-resolved luminescence-based optical sensor," Radiat. Res. **147**, 329–334 (1997).

[15]J. R. Griffiths and S. P. Robinson, "The OxyLite: A fibre-optic oxygen sensor," Br. J. Radiol. **72**, 627–630 (1999).

[16]W. K. Young, B. Vojnovic, and P. Wardman, "Measurement of oxygen tension in tumours by time-resolved fluorescence," Br. J. Cancer Suppl. **27**, S256–S259 (1996).

[17]L. Bentzen *et al.*, "Assessment of hypoxia in experimental mice tumours by [18F]fluoromisonidazole PET and pO_2 electrode measurements. Influence of tumour volume and carbogen breathing," Acta Oncol. **41**, 304–312 (2002).

[18]S. S. Foo *et al.*, "Functional imaging of intratumoral hypoxia," Mol. Imaging Biol. **6**, 291–305 (2004).

[19]W. J. Koh *et al.*, "Imaging of hypoxia in human tumors with [F-18]fluoromisonidazole," Int. J. Radiat. Oncol., Biol., Phys. **22**, 199–212 (1992).

[20]J. A. O'Donoghue *et al.*, "Assessment of regional tumor hypoxia using 18F-fluoromisonidazole and 64Cu(II)-diacetyl-bis(N4-methylthiosemicarbazone) positron emission tomography: Comparative study featuring microPET imaging, pO_2 probe measurement, autoradiography, and fluorescent microscopy in the R3327-AT and FaDu rat tumor models," Int. J. Radiat. Oncol., Biol., Phys. **61**, 1493–1502 (2005).

[21]J. A. Raleigh *et al.*, "Fluorescence immunohistochemical detection of hypoxic cells in spheroids and tumours," Br. J. Cancer **56**, 395–400 (1987).

[22]F. A. Howe *et al.*, "Issues in flow and oxygenation dependent contrast (FLOOD) imaging of tumours," NMR Biomed. **14**, 497–506 (2001).
[23]V. D. Kodibagkar *et al.*, "Novel 1H NMR approach to quantitative tissue oximetry using hexamethyldisiloxane," Magn. Reson. Med. **55**, 743–748 (2006).
[24]J. M. Brown *et al.*, "In vivo evaluation of the radiosensitizing and cytotoxic properties of newly synthesized electron-affinic drugs," Br. J. Cancer Suppl. **37**, 206–211 (1978).
[25]J. G. Rajendran and K. A. Krohn, "Imaging hypoxia and angiogenesis in tumors," Radiol. Clin. North Am. **43**, 169–187 (2005).
[26]A. R. Padhani *et al.*, "Imaging oxygenation of human tumours," Eur. Radiol. **17**, 861–872 (2007).
[27]W. J. Koh *et al.*, "Evaluation of oxygenation status during fractionated radiotherapy in human nonsmall cell lung cancers using [F-18]fluoromisonidazole positron emission tomography," Int. J. Radiat. Oncol., Biol., Phys. **33**, 391–398 (1995).
[28]D. Thorwarth *et al.*, "Combined uptake of [18F]FDG and [18F]FMISO correlates with radiation therapy outcome in head-and-neck cancer patients," Radiother. Oncol. **80**, 151–156 (2006).
[29]J. M. Arbeit *et al.*, "Hypoxia: Importance in tumor biology, noninvasive measurement by imaging, and value of its measurement in the management of cancer therapy," Int. J. Radiat. Biol. **82**, 699–757 (2006).
[30]M. Nordsmark *et al.*, "Measurements of hypoxia using pimonidazole and polarographic oxygen-sensitive electrodes in human cervix carcinomas," Radiother. Oncol. **67**, 35–44 (2003).
[31]L. Bentzen *et al.*, "Tumour oxygenation assessed by 18F-fluoromisonidazole PET and polarographic needle electrodes in human soft tissue tumours," Radiother. Oncol. **67**, 339–344 (2003).
[32]J. M. Brown, "Evidence for acutely hypoxic cells in mouse tumours, and a possible mechanism of reoxygenation," Br. J. Radiol. **52**, 650–656 (1979).
[33]D. Stoianovici *et al.*, "'MRI stealth' robot for prostate interventions," Minimally Invasive Ther. Allied Technol. **16**, 241–248 (2007).
[34]Y. Barzilay *et al.*, "Miniature robotic guidance for spine surgery—Introduction of a novel system and analysis of challenges encountered during the clinical development phase at two spine centres," Int. J. Med. Robotics Comput Assist Surg **2**, 146–153 (2006).
[35]K. Cleary *et al.*, "Precision placement of instruments for minimally invasive procedures using a 'needle driver' robot," Int. J. Med. Robotics Comput Assist Surg **1**, 40–47 (2005).
[36]S. P. DiMaio *et al.*, "Robot-assisted needle placement in open MRI: System architecture, integration and validation," Comput. Aided Surg. **12**, 15–24 (2007).
[37]J. R. Adler, Jr. *et al.*, "Image-guided robotic radiosurgery," Neurosurgery **44**, 1299–1307 (1999).
[38]P. Kazanzides *et al.*, "Development of an image-guided robot for small animal research," Comput. Aided Surg. **12**, 357–365 (2007).
[39]A. C. Waspe *et al.*, "Design, calibration and evaluation of a robotic needle-positioning system for small animal imaging applications," Phys. Med. Biol. **52**, 1863–1878 (2007).
[40]A. Ayadi *et al.*, "Fully automated image-guided needle insertion: Application to small animal biopsies," Conference Proceedings IEEE Engineering Medicine and Biology Society (IEEE, Lyon, France, 2007), Vol. 2007, pp. 194–197.
[41]P. Zanzonico *et al.*, "Animal-specific positioning molds for registration of repeat imaging studies: Comparative microPET imaging of F18-labeled fluoro-deoxyglucose and fluoro-misonidazole in rodent tumors," Nucl. Med. Biol. **33**, 65–70 (2006).
[42]A. Cherif *et al.*, "Rapid synthesis of 3-[18F]fluoro-1-(2′-nitro-1′-imidazolyl)-2-propanol ([18F]fluoromisonidazole)," Pharm. Res. **11**, 466–469 (1994).
[43]D. J. Yang *et al.*, "Development of F-18-labeled fluoroerythronitroimidazole as a PET agent for imaging tumor hypoxia," Radiology **194**, 795–800 (1995).
[44]B. Wen *et al.*, "Measurements of partial oxygen pressure (pO_2) using the OxyLite system in R3327-AT tumors under isoflurane anesthesia," Radiat. Res. **166**, 512–518 (2006).
[45]F. He *et al.*, "Noninvasive molecular imaging of hypoxia in human xenografts: Comparing hypoxia-induced gene expression with endogenous and exogenous hypoxia markers," Cancer Res. **68**, 8597–8606 (2008).
[46]J. S. Rasey *et al.*, "Characteristics of the binding of labeled fluoromisonidazole in cells in vitro," Radiat. Res. **122**, 301–308 (1990).
[47]L. I. Cardenas-Navia, T. W. Secomb, and M. W. Dewhirst, "Effects of fluctuating oxygenation on tirapazamine efficacy: Theoretical predictions," Int. J. Radiat. Oncol., Biol., Phys. **67**, 581–586 (2007).
[48]M. Zhang *et al.*, "Accuracy and reproducibility of tumor positioning during prolonged and multi-modality animal imaging studies," Phys. Med. Biol. **53**, 5867–5882 (2008).
[49]D. Thorwarth *et al.*, "A kinetic model for dynamic [18F]-FMISO PET data to analyse tumour hypoxia," Phys. Med. Biol. **50**, 2209–2224 (2005).
[50]H. Cho *et al.*, "Noninvasive multimodality imaging of the tumor microenvironment: Registered dynamic magnetic resonance imaging and positron emission tomography studies of a preclinical tumor model of tumor hypoxia," Neoplasia **11**, 247–259 (2009).
[51]J. J. Casciari, M. M. Graham, and J. S. Rasey, "A modeling approach for quantifying tumor hypoxia with [F-18]fluoromisonidazole PET time-activity data," Med. Phys. **22**, 1127–1139 (1995).
[52]W. Wang *et al.*, "Evaluation of a compartmental model for estimating tumor hypoxia via FMISO dynamic PET imaging," Phys. Med. Biol. **54**, 3083–3099 (2009).